

Multiwavelength observations of Swift J0243.6+6124 from 2017 to 2022

Wei Liu^{1,2}, Jingzhi Yan¹, Pablo Reig^{3,4}, Xiaofeng Wang^{5,6}, Guangcheng Xiao¹, Han Lin⁵, Xinhan Zhang⁵, Hanna Sai⁵, Zhihao Chen⁵, Shengyu Yan⁵, and Qingzhong Liu¹

¹ Key Laboratory of Dark Matter and Space Astronomy, Purple Mountain Observatory, Chinese Academy of Sciences, Nanjing, 210023, China

e-mail: weiliu@pmo.ac.cn, jzyan@pmo.ac.cn

² School of Astronomy and Space Science, University of Science and Technology of China, Hefei, 230026, China

³ Institute of Astrophysics, Foundation for Research and Technology-Hellas, 71110 Heraklion, Greece

⁴ Physics Department, University of Crete, 71003 Heraklion, Greece

⁵ Physics Department/Tsinghua Center for Astrophysics, Tsinghua University, Beijing, 100084, China

⁶ Beijing Planetarium, Beijing Academy of Sciences and Technology, Beijing, 100044, China

Received 27 May 2022 / Accepted 12 July 2022

ABSTRACT

Context. Swift J0243.6+6124 is a high-mass X-ray binary that went into a giant X-ray outburst in 2017. During this event, the X-ray luminosity reached the highest value ever measured in a galactic Be/X-ray binary.

Aims. Our aim is to study the long-term variability of Swift J0243.6+6124 after the 2017 major X-ray outburst.

Methods. We have obtained optical spectroscopy and photometry data during four years after the event. The long-term photometric light curve and the equivalent widths of the H α and He I λ 6678 lines were used to monitor the state of the Be star's circumstellar disk. The H α line profiles show evidence for V/R variability that was accounted for by fitting the H α spectral line profile with two Gaussian functions. We divided our data into three phases according to the intensity of the X-ray, optical, and infrared emission.

Results. Phase I covers the rise and decay of the giant X-ray outburst that took place in October–November 2017. We interpret phase II as the dissipation of the Be star's equatorial disk and phase III as its recovery. The timescale of a complete formation and dissipation process is about 1250 days. The epoch when the dissipation process stopped and the reformation period began is estimated to be around MJD 58530. We find a delay of ~ 100 – 200 days between the minimum of the optical or infrared intensity and the strength of the H α line after the X-ray outburst, which may indicate that the dissipation of the disk begins from the inner parts. The motion of the density perturbation inside the disk is prograde, with a V/R quasi-period of about four years. The source shows a positive correlation in the $(B - V)$ color index versus V -band magnitude diagram, which implies that the system is seen at a small or moderate inclination angle.

Conclusions. Despite the super-Eddington X-ray luminosity during the outburst, the subsequent pattern of long-term optical and IR variability of Swift J0243.6+6124 is typical of Be/X-ray binaries.

Key words. stars: emission-line, Be – binaries: close – X-rays: binaries – stars: individual: Swift J0243.6+6124 – stars: neutron

1. Introduction

According to the luminosity class of the optical companion, high-mass X-ray binaries (HMXBs) are divided into supergiant X-ray binaries and Be/X-ray binaries (BeXBs; Reig 2011). Most of the optically identified HMXBs (or HMXB candidates) are known or suspected BeXBs (Liu et al. 2006). The optical companion of a BeXB is a Be star, which is a nonsupergiant, fast-rotating B-type (but it may also include late O-type stars; Negueruela et al. 2004), and luminosity class III–V star that has shown emission lines at some point in its life (Rivinius et al. 2013). There are two different disks in Be/X-ray binaries: circumstellar disks around the Be stars, and accretion disks around the neutron stars, which temporarily appear during X-ray outbursts (Ziolkowski 2002; Hayasaki & Okazaki 2004). BeXBs are classified into persistent and transient sources according to their X-ray properties (Reig & Roche 1999). Transient BeXBs display two types of X-ray outbursts when they are active: type I (or normal) outbursts, and type II (or giant) outbursts. The peak luminosity during type I outbursts is typically $L_X \leq 10^{37}$ erg s⁻¹,

while during type II outbursts, it may reach the Eddington limit, $L_X \sim 10^{38}$ erg s⁻¹.

Swift J0243.6+6124 was detected in X-rays for the first time by the *Swift*/BAT on 3 October 2017 (Kennea et al. 2017). It is the first Be/X-ray binary emitting at super-Eddington luminosity in our galaxy. Reig et al. (2020) estimated the spectral type and rotational velocity of the companion of Swift J0243.6+6124 to be O9.5Ve and $v \sin i = 210 \pm 20$ km s⁻¹. X-ray pulsations with a period of ~ 9.86 s were detected by *Swift*/XRT and *Fermi*/GBM (Jenke & Wilson-Hodge 2017). The orbital period is 28.3 days, and the eccentricity is 0.092 (Doroshenko et al. 2018).

There are several different reported values for the distance to this source in the literature: 2.5 ± 0.5 kpc (Bikmaev et al. 2017) and ~ 5 kpc (Reig et al. 2020), both based on optical photometric observations, a lower limit of 5 kpc set by van den Eijnden et al. (2018), ~ 6 kpc based on two accretion torque models (Zhang et al. 2019), and $5.5^{+0.4}_{-0.3}$ kpc given in *Gaia* DR3 catalog (*Gaia* Collaboration et al. 2016; 2022). If the distance of the source is assumed for 5 kpc, its peak luminosity is estimated as 1×10^{39}

erg s⁻¹ (0.1–10 keV). This exceeds the Eddington limit for the neutron star during the giant outburst.

The magnetic field strength of the neutron star in Swift J0243.6+6124 is estimated to be approximately 10¹³ G (Tsygankov et al. 2018; Zhang et al. 2019), although Doroshenko et al. (2018) advocated for a lower value, at the lower limit of the range (3 – 9) × 10¹² G. Based on the detection of electron-cyclotron resonance scattering features (CRSFs), Kong et al. (2022) estimated a surface magnetic field of ~ 1.6 × 10¹³ G for Swift J0243.6+6124, which unambiguously proves the presence of multipole field components close to the surface of the neutron star. This measured surface magnetic field is the strongest of all known neutron stars with detected electron CRSFs, and it is also the strongest for all neutron star ultraluminous X-ray sources. All types of X-ray binaries have been observed to launch jets, with the exception of neutron stars that have strong magnetic fields (stronger than 10¹² G), which implies that their magnetic field strength restrains jet formation (van den Eijnden et al. 2018). Therefore, the detection of radio emission from Swift J0243.6+6124 during the X-ray outbursts is a surprising result. However, the radio luminosity is two orders of magnitude dimmer than those seen in other accreting neutron stars with similar X-ray luminosities (van den Eijnden et al. 2018), which implies that the magnetic field of neutron stars still plays an important role in the power of launching jets. In this work, we report new optical spectroscopic observations and photometric observations. These observations witnessed the partial dissipation after the giant outburst and subsequent reformation of the Be star’s circumstellar disk.

2. Observations

2.1. Optical spectroscopy

Optical spectroscopic observations were mainly obtained with two telescopes at two different observatories: The observations from the Xinglong Station of National Astronomical Observatories in Hebei province (China) were obtained with the spectrometer OptoMechanics Research (OMR) or BAO Faint Object Spectrography and Camera (BFOSC) on the 2.16 m telescope, and the observations from the Lijiang station of Yunnan Astronomical Observatory in Yunnan province (China) used the spectrometer Yunnan Faint Object Spectrography and Camera (YFOSC) on the 2.4 m telescope. The OMR was equipped with a 1024 × 1024 (24 micron) pixel TK1024AB2 CCD. The OMR Grism 4 is 1200 lp mm⁻¹, giving a nominal dispersion of 1.2 Å pixel⁻¹, and covering the wavelength ranges 5500–6900 Å. The BFOSC was equipped with a 2048 × 2048 (15 micron) pixel Loral Lick 3 CCD. The dispersion of BFOSC Grism 4 and 8 is 2.97 and 1.20 Å pixel⁻¹, covering the wavelength ranges 4000–8700 and 5800–8280 Å, respectively. The YFOSC was equipped with a 2k × 4k (13.5 micron) pixel E2V 42-90 CCD. The dispersion of YFOSC Grism 8 is 1.47 Å pixel⁻¹, covering the wavelength ranges 4970–9830 Å. In addition, we analyzed new optical spectroscopic observations obtained from the 1.3 m telescope of the Skinakas observatory (SKO) in Crete (Greece). The 1.3 m telescope of the SKO was equipped with a 2048 × 2048 (13.5 micron) pixel ANDOR IKON CCD and a 1302 lines mm⁻¹ grating, giving a nominal dispersion of ~ 0.8 Å pixel⁻¹.

We used the Image Reduction and Analysis Facility (IRAF)¹ software package to reduce and analyze all the spectra, performing bias-subtracted correction and flat-field correction on the data, and then removing cosmic rays. A helium-argon calibration lamp was employed to obtain the pixel-wavelength relation. In order to ensure the consistency of spectral processing, all spectra were normalized to adjacent continua. We measured the equivalent width of the H α lines (hereafter EW(H α) for short) for five times, each measurement with a different selection of the continuum. The final EW(H α) is the average of the five measurements, and the error is the standard deviation. The typical error of EW(H α) is within 5%. The value of the error is determined by the quality of the continuum. The equivalent widths of the He I λ 6678 lines (hereafter EW(He I λ 6678) for short) were obtained following the same method as for EW(H α).

The log of the spectroscopic observations is given in Table A.1. EW(He I λ 6678) and EW(H α) are plotted in the third and sixth panels of Fig. 1, respectively. The evolution of the H α line profiles is plotted in Fig. 3. The evolution of the log(V/R) and the peak separation of H α line are plotted in Fig. 4 and listed in Table B.1.

2.2. Optical photometry

Optical photometric observations were obtained from five telescopes at three different observatories: From the Xinglong station of the National Astronomical Observatories, Chinese Academy of Sciences (NAOC), observations were obtained with the Tsinghua-NAOC Telescope (TNT, 80 cm), the 60 cm telescope, and the 2.16 m telescope; from the Lijiang station of Yunnan Observatories (YNAO), the data came from the 2.4 m telescope; and from the Yaoan astronomical observation station of Purple Mountain Observatory (PMO), the data came from the Yaoan High Precision Telescope (YAHPT, 80 cm’).

The TNT (80 cm) is an equatorial-mounted Cassegrain system with a focal ratio of f/10, made by AstroOptik, funded by Tsinghua University in 2004 and jointly operated with NAOC, which is equipped with a PI VersArray 1300B LN 1340 × 1300 thin, back-illuminated CCD with a 20 μ m pixel⁻¹ size (Wang et al. 2008; Huang et al. 2012). In this configuration, the plate scale is 0.52" pixel⁻¹ and gives a field of view of 11.4 × 11.1 arcmin². The 60 cm telescope is an equatorial-mounted system with a focal ratio of f/4.23, which is equipped with the Andor DU934P-BEX2-DD 1024 × 1024 CCD and provides a field of view of 18 × 18 arcmin². The 2.4 m telescope is an altazimuth-mounted Cassegrain system with a focal ratio of f/8, which is equipped with an E2V CCD42-90 2k × 2k thin, back-illuminated, deep-depletion CCD with a 13.5 μ m pixel⁻¹ size. In this configuration, the plate scale is 0.28" pixel⁻¹ and gives a field of view of 9.6 × 9.6 arcmin². The YAHPT (80 cm’) is an altazimuth-mounted, RC optical system with a focal ratio of f/10, made by Astro Systeme Austria, which is equipped with a PIXIS 2048B back-illuminated CCD with a 13.5 μ m pixel⁻¹ size. In this configuration, the plate scale is 0.347" pixel⁻¹, providing a field of view of 11.8 × 11.8 arcmin². The 2.16 m telescope is an equatorial-mounted, RC optical system with a focal ratio of f/9, made by NAOC, CAS Nanjing Astronomical Instruments Co., LTD (NAIRC), and the Institute of Automation of the Chinese Academy of Sciences (CASIA), which is equipped with an Andor-DZ936-BEX2-DD 2048 × 2048 CCD with a 13.5

¹ IRAF is distributed by NOAO, which is operated by the Association of Universities for Research in Astronomy, Inc., under cooperation with the National Science Foundation.

$\mu\text{m pixel}^{-1}$ size. In this configuration, the plate scale is $0.274'' \text{ pixel}^{-1}$, providing a field of view of $9.36 \times 9.36 \text{ arcmin}^2$.

In all five telescopes, Swift J0243.6+6124 was observed through the standard Johnson-Cousins *B*, *V*, *R*, and *I* filters. The photometric data reduction was performed using standard routines and aperture photometry packages (some from the *zphot* package) in IRAF, including bias subtraction and flat-field correction. In order to derive the variation in the optical brightness, we selected the reference star Gaia 465628266540345216 (α : 02 43 38.23, and δ : +61 26 40.7, J2000) (according to Reig et al. 2020, the average magnitudes of the reference star are $B = 13.67 \pm 0.01$, $V = 13.02 \pm 0.01$, $R = 12.65 \pm 0.01$, and $I = 12.25 \pm 0.02$) in the field of view of Swift J0243.6+6124 to derive its differential magnitudes. The photometric magnitudes are given in Table C.1.

To study the long-term optical variability of the source, we used the public optical photometric data from the ASAS-SN² Variable Stars Database (Shappee et al. 2014; Jayasinghe et al. 2019). There is a slightly fainter star at 6.2 arcsec from Swift J0243.6+6124 within the full width at half maximum (FWHM). This star is resolved in our photometry. However, the pixel scale and the FWHM in ASAS-SN are 8 arcsec and ~ 2 pixels, and hence in these images, the neighboring star contributes to the measured flux from Swift J0243.6+6124. The calibrated *V*-band magnitude of the fainter close star is $V = 14.52 \pm 0.01 \text{ mag}$ (Reig et al. 2020). We removed the brightness of the neighboring star from the total observed flux. The applied corrections are in the range $\Delta V = 0.20^{+0.03}_{-0.04} \text{ mag}$. We also made use of the public optical photometric data from the international database of the American Association of Variable Star Observers (AAVSO³). Finally, we also included the optical photometric data from Reig et al. (2020).

The Johnson *V*-band light curve is plotted in the fourth panel of Fig. 1. A detailed view of the 2017 outburst, including pre- and post-outburst observations, is shown in Fig. 2. The evolution of the (*B* – *V*) color index is plotted in the seventh panel of Fig. 1, and the variation of the (*B* – *V*) color index versus *V*-band magnitude is plotted in Fig. 5, where only the data from the 80 cm telescope, the 2.4 m telescope, and the 2.16 m telescope are shown.

2.3. NEOWISE photometry

We made use of the light curves in the W1 (3.4 μm) and W2 (4.6 μm) bands provided by the NEOWISE (Mainzer et al. 2011) project through the IRSA viewer⁴. We plot them in the fifth panel of Fig. 1 and in the bottom panel of Fig. 2.

2.4. X-Ray observations

The Burst Alert Telescope (BAT)⁵ on board *Swift* (Krimm et al. 2013), *MAXI*⁶, and the Gamma-ray Burst Monitor (GBM)⁷ on board *Fermi* (Meegan et al. 2009) have been monitoring Swift

J0243.6+6124 in the hard X-ray energy band (15–50 keV with BAT, 2–20 keV with *MAXI*, and 12–50 keV with GBM) since October 2017. One type II X-ray outburst and several type I outbursts were detected between October 2017 and January 2019. The X-ray band light curves from BAT (15–50 keV) and *MAXI* (2–20 keV) are plotted in the first panel of Fig. 1. The spin-frequency history measured with GBM is plotted in the second panel of Fig. 1.

3. Results

Figure 1 shows the X-ray, optical, and IR long-term variability of Swift J0243.6+6124. The observations cover the October 2017 X-ray outburst and the changes experienced by the source during the following four-year period. After the X-ray outbursts, the optical brightness of the source decreased and reached a minimum on $\sim \text{MJD } 58530$. Since then, it has been recovering. There is a clear correlation between the optical and IR flux on long timescales (weeks or months). When the source is active in the X-ray, the optical and IR also correlate with the overall X-ray flux in the sense that the source is bright in the optical and IR at the time of the outbursts. The strength of the $H\alpha$ line also follows the same general trend, although the minimum after the X-ray outbursts appears to be delayed by ~ 100 – 200 days with respect to the optical or IR continuum flux.

After examining the long-term light curves and spectral evolution, we divided the observations into three different epochs or phases (Fig. 1). These phases reflect significant changes in the properties of the data. Each phase is characterized by a different pattern of X-ray, optical, or IR variability. Phase I corresponds to the giant 2017 X-ray outburst; during phase II, the source experiences a gradual fading of its brightness and a weakening of the spectral line parameters; and in phase III, the long-term trend is reversed and the source exhibits a gradual increase in the brightness and strength of the spectral lines, most significantly, in the $H\alpha$ line.

Phase I (MJD 58030–58180) covers the giant X-ray outburst. The X-ray luminosity changes by about two orders of magnitude ($10^{37} - 10^{39} \text{ erg s}^{-1}$; Doroshenko et al. 2020) and the *V* band by 0.4 magnitudes. $\text{EW}(H\alpha)$ and $\text{EW}(\text{He I } \lambda 6678)$ display erratic variability. The (*B* – *V*) color displays the largest variation in the entire period of the observations, with a change of about 0.1 magnitude in 25 days.

In Phase II (MJD 58180–58530), the X-ray variability is characterized by regular type I outbursts with changes in luminosity of about one order of magnitude between $10^{36} - 10^{37} \text{ erg s}^{-1}$. The brightness in the *V* band decreases by 0.1 magnitudes and in the near-infrared by 0.6 magnitudes. $\text{EW}(H\alpha)$ decreases from a maximum of -11 \AA to a minimum of -5 \AA . $\text{EW}(\text{He I } \lambda 6678)$ presents large scatter, but it also decreases on average. The dispersion in $\text{EW}(\text{He I } \lambda 6678)$ measurements is most likely due to the low signal-to-noise ratio (S/N). There are no suitable *B*-band observations during the first half of this phase; thus we do not have (*B* – *V*) data. During the second half, the (*B* – *V*) color is lower on average (i.e., bluer emission) than during phase I.

In Phase III (MJD 58530–), the source is no longer detected in X-ray, while all optical and infrared indicators increase gradually. At the end of this phase, $\text{EW}(H\alpha)$ and the *V*-band magnitude recover to almost pre-outburst values. The overall optical emission becomes redder as the system evolves in this phase.

² <https://asas-sn.osu.edu/variables/7306192e-fb93-58a1-98a8-1809e318a711>

³ https://app.aavso.org/webobs/results/?star=000-BML-322&num_results=200

⁴ <https://irsa.ipac.caltech.edu/irsaviewer>

⁵ <https://swift.gsfc.nasa.gov/results/transients/weak/SwiftJ0243.6p6124/>

⁶ http://maxi.riken.jp/star_data/J0243+614/J0243+614.html

⁷ <https://gammaray.nsstc.nasa.gov/gbm/science/pulsars/lightcurves/swiftj0243.html>

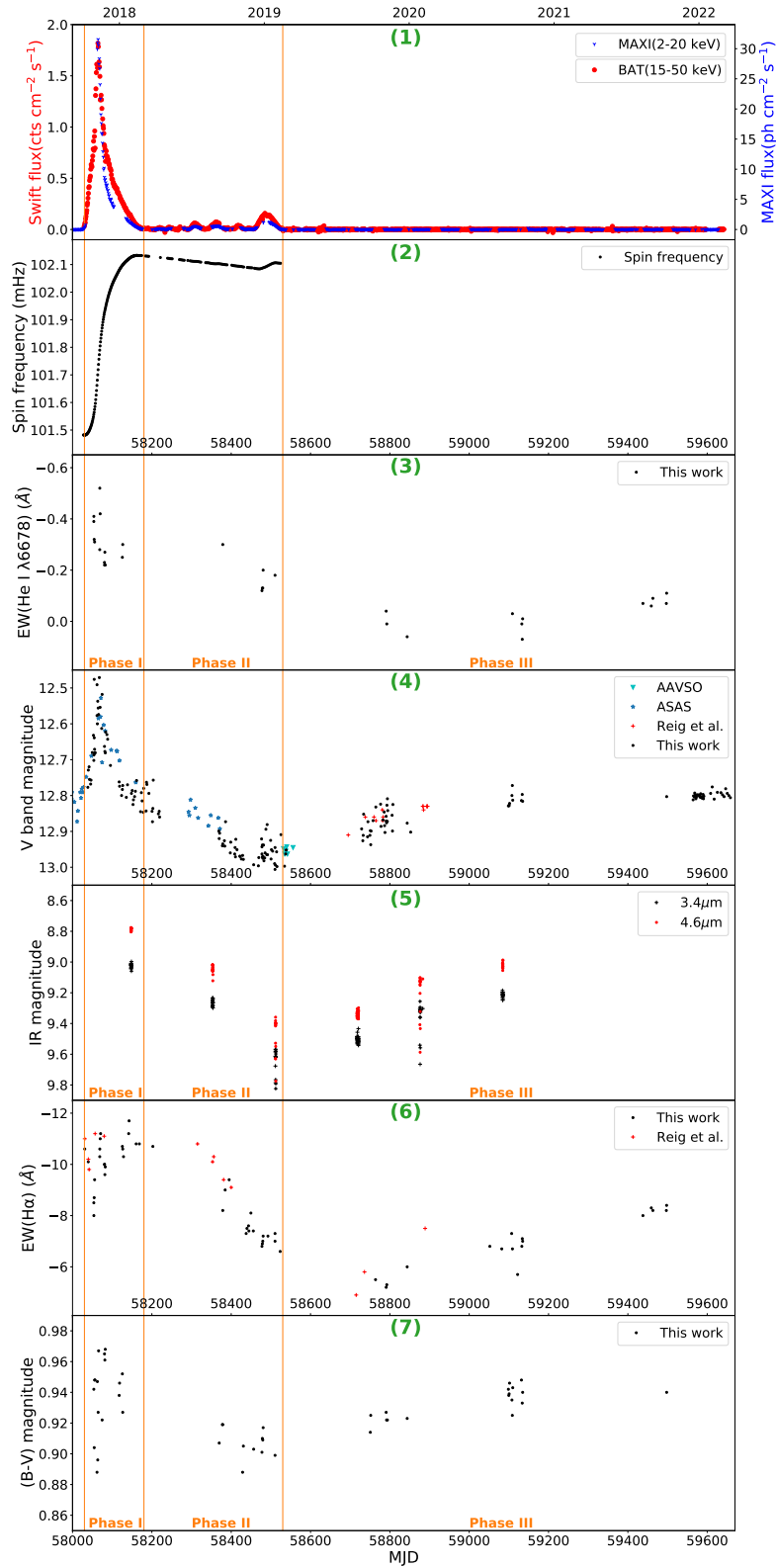


Fig. 1. Long-term variations of Swift J0243.6+6124 from 2017 to 2022. First panel: X-ray band light curves. The data from *Swift*/BAT (15–50 keV) and *MAXI* (2–20 keV) are labeled with red points and blue downward triangles, respectively. The first day of each year is also marked at the top of the first panel in the format YYYY. Second panel: Barycentered and orbit-corrected spin-frequency history measured with *Fermi*/GBM. Third panel: Equivalent widths of He I $\lambda 6678$ lines. Fourth panel: Long-term light curves of the optical *V* band from *AAVSO*, *ASAS-SN*, Reig et al. (2020), and this work. They are separately labeled with light green downward triangles, blue stars, red plus signs, and black points. Fifth panel: Long-term light curves of *NEOWISE* infrared magnitudes at $3.4 \mu\text{m}$ and $4.6 \mu\text{m}$. They are labeled with black plus signs and red points, respectively. Sixth panel: Equivalent widths of $\text{H}\alpha$ lines from this work and Reig et al. (2020). They are labeled with black points and red plus signs, respectively. Seventh panel: Evolution of the $(B - V)$ color index. The vertical lines separate the three phases into which the observations are divided.

3.1. $H\alpha$ line profiles

Figure 3 shows the profiles of the $H\alpha$ line. Although we are limited by the low spectral resolution, some general variability trends are visible. The $H\alpha$ emission lines present asymmetrically blue-dominated profiles ($V > R$) between October 2017 and September 2018 (phase I–phase II). The red peak is only noticeable in the earliest spectrum on 27 October 2017. The central rest wavelength (marked by the vertical dashed line in Fig. 3) lies systematically to the right of the peak, confirming the asymmetry. At the end of 2018 and during 2019 (phase II–phase III), the line flux gradually shifts toward the red. Approximately symmetric single-peak profiles are observed in the 2020–2021 spectra (phase III). At the end of 2021, the profiles are again blue-dominated.

The He I line also exhibits a variable asymmetric double-peak profile in phase and with intensity variations similar to those of the $H\alpha$ line. Because the He I line forms much closer to the Be star than the $H\alpha$ line, the He I V/R variability implies that the density perturbation affects the inner parts of the disk as well as the outer parts where the $H\alpha$ line is formed. Unfortunately, the low S/N and low spectral resolution prevented a detailed analysis of this line.

4. Discussion

We have been monitoring the optical counterpart of the Be/X-ray binary Swift J0243.6+6124 since its discovery in October 2017 and obtained optical spectra on a regular basis. Using data from both the archives and the literature, we are able to study the long-term variability over at least four years after the outburst. We attribute this long-term variability to the evolution of the Be star’s circumstellar disk.

The variability patterns of the X-ray, optical, and IR parameters allowed us to divide the observations into three different phases. Phase I covers the rise and decay of the X-ray outburst. The largest and fastest variability timescales are seen during this phase. This violent event must have affected the entire structure of the circumstellar disk. In particular, the $H\alpha$ line displayed several sudden changes of 10%–20% in its strength on timescales of about one month during this phase (see the sixth panel of Fig. 1). These fast changes could be attributed to an inhomogeneous warped disk (Reig et al. 2020). Alternatively, because the fast changes of $EW(H\alpha)$ appear to be modulated with the orbital period of the system ($P_{\text{orb}} = 28.3$ days), reprocessed emission might be at their origin. The high spin-up rate (as seen in the second panel of Fig. 1) suggests that a short-lived accretion disk also formed around the neutron star.

Phase II corresponds to a low optical state in which not only the optical and IR continuum flux gradually decreased, but the $H\alpha$ emission line also became weaker. Type II outbursts involve the accretion of a large amount of material from the equatorial disk and almost always lead to the dissipation of the entire or part of the disk (Reig et al. 2016). We identify this phase with the dissipation of the disk. The evolution of the X-ray and optical emissions provides some clues about how this dissipation took place. The presence of type I outbursts indicates that the neutron star accretes material from the disk in subsequent periastron passages, while at the same time, the decrease in the $(B - V)$ color indicates that the emission becomes bluer, as expected from a smaller or more compact disk. These results can be understood if the outer parts of the disk cease to be bound, that is, are expelled, while the inner parts of the disk collapse toward the star once the disk formation mechanism stops. The higher X-ray in-

tensity of the last type I outburst in this phase may be due to the fact that the neutron star encountered a higher-density part of this distorted disk. This phase ends when the magnitude and colors reach a minimum. The system did not lose the disk entirely, as the $H\alpha$ line remained with an emission profile and the minimum $EW(H\alpha)$ was still ~ -5 Å. Even the He I $\lambda 6678$ did not revert into an absorption profile. The equivalent width of this line remained ~ 0 Å during 2020 and 2021, indicating that the line was filled with emission.

Phase III represents a phase in which the disk grew again. The optical and IR flux increased, as did the strength of the $H\alpha$ line. The overall emission became redder (i.e., $(B - V)$ increased). The latest observations show that $EW(H\alpha)$ and $EW(\text{He I } \lambda 6678)$ approached pre-outburst values. After an initial brightening period that lasted for about a year, the V -band magnitude stabilized at a level of 12.8^m , at which it has remained since September 2020.

Photometric variability with a characteristic period of ~ 1250 days (MJD 40000–41250) and an amplitude of ~ 0.15 magnitudes in the B band was reported by Nesci (2017) based on archival data from the Asiago Observatory taken between 1967 and 1976. This timescale is similar to the one during MJD 57250 to 58530 (see Fig. 2). When the V -band flare is ignored, the underlying trend of the V -band observations correlates very well with the IR-band observations. Given the strength of this correlation, the lack of a similar flare in the IR light curve can be attributed to the low cadence of the IR observations. The disk starts to grow on \sim MJD 57250, reaching a maximum size on \sim MJD 58000 when it begins to decline, and reaching a minimum on \sim MJD 58530. The variation in the V/IR -band can be interpreted in terms of the evolution of the Be star’s disk. This long-term smooth change in brightness is due to the formation or growth of the disk and its subsequent dissipation. We estimate that the overall timescale in phase III for the formation and dissipation of the circumstellar disk is about 1500 days. The dissipation phase is significantly faster, about 300 days, than the formation phase of about 1200 days.

Although the evolution of the optical and IR parameters is affected by observational gaps, because the position of the source is too close to the Sun, Fig. 1 shows a delay between the minima of the optical and IR continuum (which marks the shift from phase II to phase III) and the minima of $EW(H\alpha)$. This delay may be understood by invoking the different sites of the continuum and discrete emission in the equatorial disk of a Be star. According to Carciofi (2011), the disk V band is typically formed very close to the star, within about $2R_{\text{star}}$. In contrast, the $H\alpha$ emission line is formed at larger radii (Slettebak et al. 1992). If this interpretation is correct, then the minimum flux detected in the continuum first would imply that the dissipation of the disk began from the inner parts. The type I regular X-ray outbursts during phase II indicate that the accretion of the neutron star persisted for about one year after the main outburst. In terms of the strength of the $H\alpha$ line, the giant X-ray outburst took place when $EW(H\alpha) \sim -11$ Å. The increase rate of $EW(H\alpha)$ during phase III implies that the source will reach this value again on \sim MJD 60250. If we take this value (-11 Å) as the triggering value of the giant outburst, then we should expect another large event by the end of 2023.

The He I $\lambda 6678$ follows the same long-term trend as the $H\alpha$ line: fast and large amplitude changes during phase I, a weakening during phase II, and a slow recovery during phase III. The latest spectrum in October 2021, in which a small peak started to develop and $EW(\text{He I } \lambda 6678) < -0.1$ Å, marks the formation

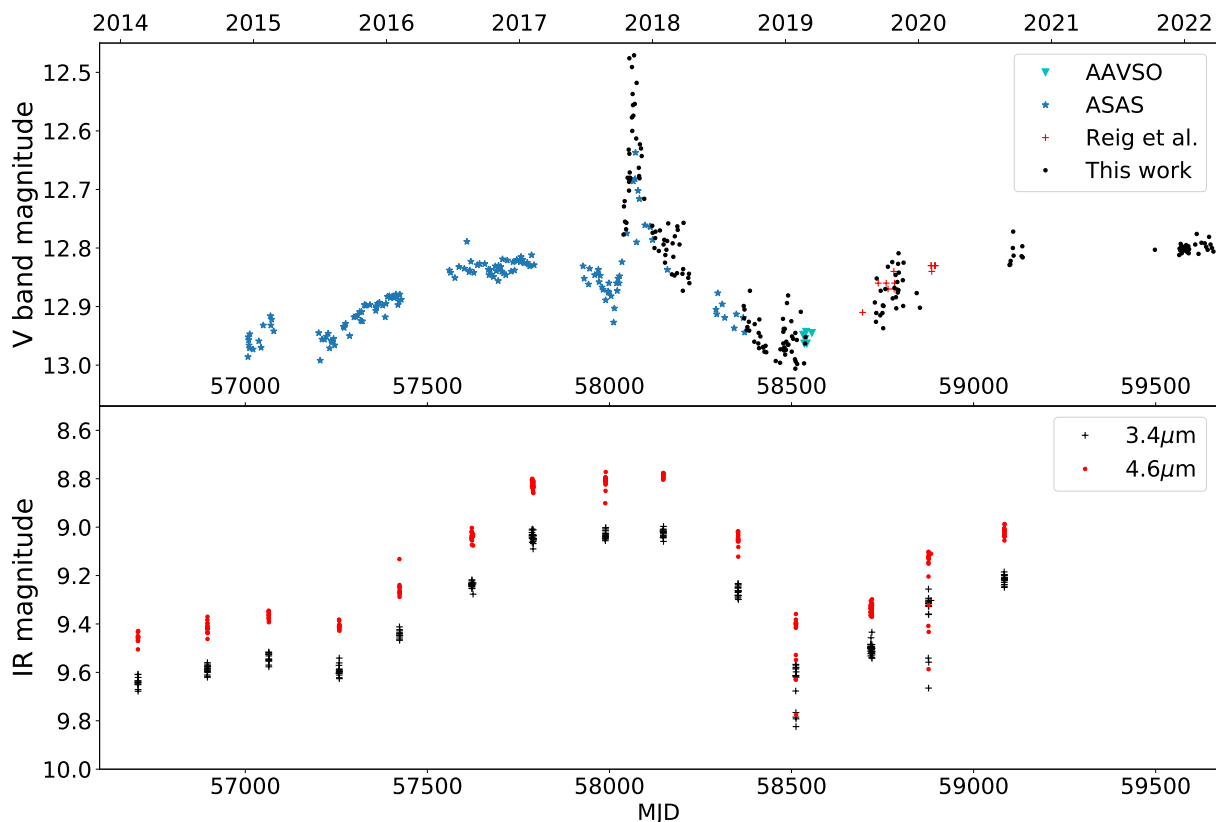


Fig. 2. Multiwavelength light curves of Swift J0243.6+6124. Top panel: Long-term light curves of the optical V band from MJD 56600 to 59670. Bottom panel: Simultaneous light curves of *NEOWISE* infrared magnitudes at $3.4 \mu\text{m}$ and $4.6 \mu\text{m}$.

of a new emission line. We note that the giant X-ray outburst occurred when $\text{EW}(\text{He I } \lambda 6678) \sim -(0.2 - 0.5) \text{ \AA}$.

4.1. $H\alpha$ line profile variability and V/R ratio

The V/R variability is defined as the intensity variations of the two peaks (known as violet and red peaks) in the split profile of a spectral line. In many Be stars, if they are monitored over a long enough period of time, these variations are quasi-periodic (Okazaki 1997). We define the V/R ratio of the $H\alpha$ line as $V/R = (I(V) - I_c) / (I(R) - I_c)$, where $I(V)$, $I(R)$, and I_c are the intensities of the violet peak, red peak, and continuum, respectively. We also measured the separation of the violet and red peaks by fitting two Gaussian functions to the spectral line profile. When the disk velocity is assumed to be Keplerian, the peak separation gives a measure of the velocity field. There is no obvious trend in the peak separation between different spectral line profiles, which is mainly distributed around $175\text{--}250 \text{ km s}^{-1}$. The V/R ratios and the peak separation of the $H\alpha$ line are listed in Table B.1 and plotted in Fig. 4.

The V/R variability has been associated with density perturbations in the disk (Hanuschik et al. 1995). When this density perturbation moves around inside the disk, the profile changes. We observe a blue-dominated profile ($V > R$) in 2017 that turned into an almost single peak profile ($V \sim R$) in 2018 (see Fig. 4 of Reig et al. 2020), and a red-dominated profile ($V < R$) from the end of 2018 to 2019. The spectra in 2021 return to blue-dominated profiles ($V > R$). Thus, we may have covered an entire

V/R cycle. The V/R quasi-period would be about four years, which is normal for BeXBs (Mennickent et al. 1997).

In principle, the question of whether the motion of the perturbation occurs in the same sense (prograde rotation) or opposite sense (retrograde rotation) to the stellar rotation can be determined from the observations. Telting et al. (1994) realized that a prograde rotation implies that (I) a $V > R$ phase, (II) a shell absorption profile, (III) a $V < R$ phase, and (IV) a weak central absorption profile will appear in order. A retrograde rotation would give rise to the reversed sequence: (IV) \rightarrow (III) \rightarrow (II) \rightarrow (I). Because of the small disk inclination (Reig et al. 2020), we cannot distinguish a prograde or retrograde rotation in the characteristic line shapes. These characteristic line shapes can translate into noticeable photometric variations, however. According to Mennickent et al. (1997), we can expect a minimum brightness when $V = R$ prior to the $V < R$ ($V > R$) phase if the motion is prograde (retrograde). In Swift J0243.6+6124, the minimum brightness in the photometric V band occurred during the $V = R$ phase before the $V < R$ phase began, \sim MJD 58450, confirming the prograde nature of the precession inside the disk.

4.2. Variation in $(B - V)$ color index and inclination of the Be star's disk

Figure 5 shows the $(B - V)$ color index as a function of the V magnitude. We mark the different variability phases defined above with different colors. It has been noted that this kind of plot can be used to constrain the inclination angle of the system (Harmanec 1983). Systems that show a positive correlation, that

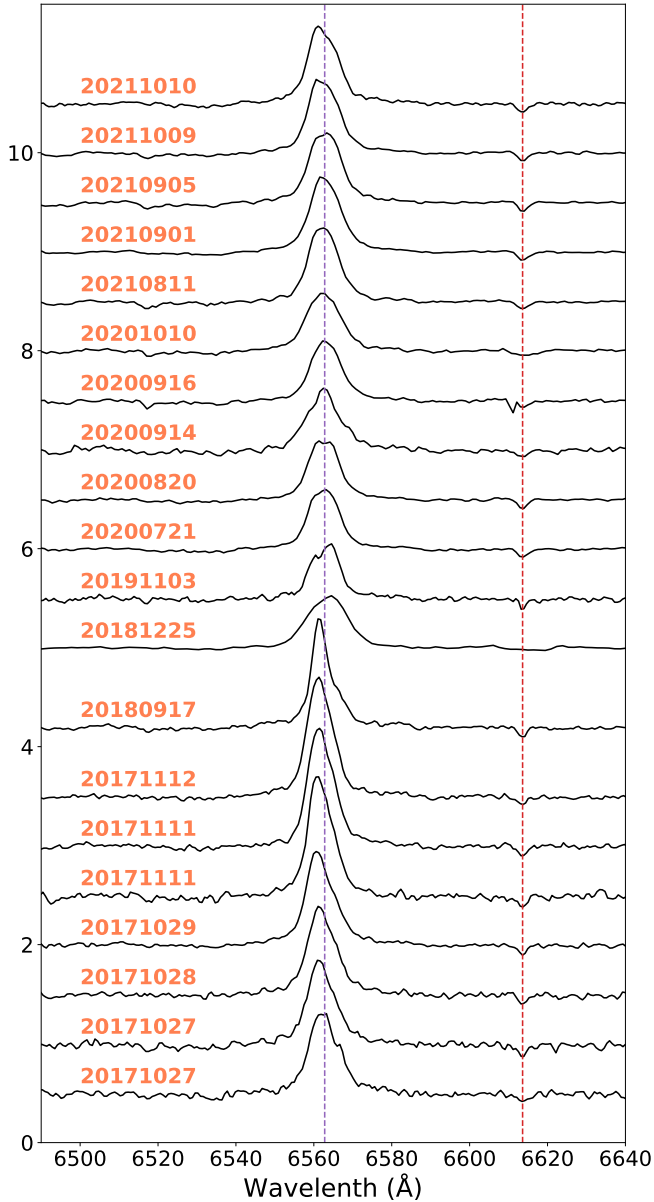


Fig. 3. Evolution of $H\alpha$ line profiles. The vertical lines mark the rest wavelength of the $H\alpha$ lines and diffuse interstellar bands (DIB) 6613 Å. All spectra have been normalized with adjacent continua.

is, as the disk forms (or equivalently, as $EW(H\alpha)$ increases), the optical intensity increases and the emission becomes redder (i.e., $(B - V)$ increases), are thought to be seen at small or moderate inclination angles, while systems that show a negative correlation, in which the optical intensity decreases even though the disk is growing ($EW(H\alpha)$ and $(B - V)$ increase), are associated with large inclination angles.

Harmanec (1983) introduced the concept of a pseudophotosphere to explain this effect. At large inclination angles (for equator-on stars), the inner parts of the Be envelope partly block the stellar photosphere, and thus the optical brightness decreases. Meanwhile, the overall emission becomes redder because the contribution of the disk increases. At small or intermediate inclination, as the disk grows, an overall (star plus disk) increase in brightness is expected.

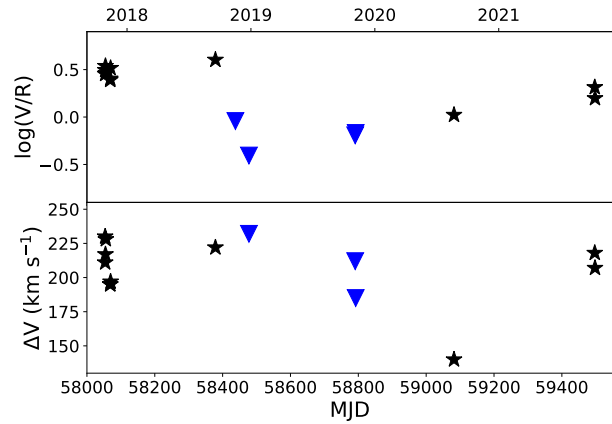


Fig. 4. Variations in spectral features of $H\alpha$ line. Top panel: Evolution of $\log(V/R)$. Bottom panel: Peak separation of $H\alpha$ line. Stars represent the spectral profiles with $V > R$, and triangles represent the spectral profiles with $V < R$.

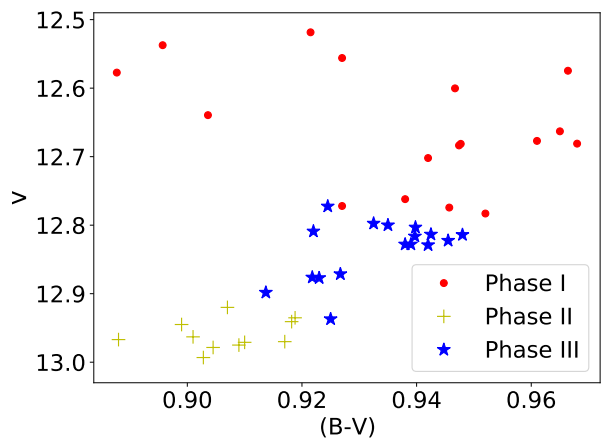


Fig. 5. Variation in $(B - V)$ color index versus V -band magnitude.

Figure 5 suggests that Swift J0243.6+6124 is viewed at small or intermediate angles. This result is consistent with the 30° angle estimated by Reig et al. (2020) from the emission-line profile.

5. Conclusions

We have conducted spectroscopic and photometric observations of Swift J0243.6+6124 to study the changes in the structure of the circumstellar disk of the Be star and the material transfer between the Be star's circumstellar disk and the neutron star during 2017–2022. This period covers a giant X-ray outburst (type II) and several orbit-modulated outbursts (type I). We divided our data into three phases based on the intensity of the X-ray, optical, and infrared emission. Phase I covers the 2017 X-ray outburst. In this phase, the source reaches the largest equivalent width of the $H\alpha$ and He I $\lambda 6678$ lines and the brightest X-ray, optical, and infrared intensity, characterized by outbursts or flares. In phase II, the source displays a long-term decrease in the optical and infrared intensities. The X-ray band is characterized by the occurrence of several minor orbit-modulated outbursts. In phase III, the source exhibits a long-term brightening of the optical and infrared magnitudes, and the equivalent width of the $H\alpha$ and He I $\lambda 6678$ lines also increases. During this phase, no X-ray activity is observed. We focused on the correlated optical, IR, and X-ray

long-term variability. During the period of our observations following the giant X-ray outburst, the optical and IR continuum flux and the strength of the H α line first decreased and then increased. We interpret this long-term variability in terms of the dissipation and reformation of the Be star's circumstellar disk. Although the 2017 giant X-ray outburst is the most luminous ever recorded in a BeXB, it does not lead to the complete loss of the Be star's disk. We estimate that at the rate at which the disk is reforming, the equivalent width of the H α line will reach pre-outburst values in about 1–1.5 years.

Acknowledgements. We acknowledge the support of the staff of the Xinglong 2.16 m telescope, the Xinglong 80 cm telescope, and the Xinglong 60 cm telescope. This work was partially supported by the Open Project Program of the CAS Key Laboratory of Optical Astronomy, National Astronomical Observatories, Chinese Academy of Sciences. We acknowledge the support of the staff of the Lijiang 2.4 m telescope. Funding for the telescope has been provided by CAS and the People's Government of Yunnan Province. Skinakas Observatory is run by the University of Crete and the Foundation for Research and Technology-Hellas. This research has made use of data provided by the Yaoan High Precision Telescope. We acknowledge with thanks the variable star observations from the *AAVSO* International Database contributed by observers worldwide and used in this research. *Swift*/BAT transient monitor results provided by the *Swift*/BAT team. *Fermi*/GBM results provided by the Fermi Science Support Center. This publication makes use of data products from *NEOWISE*, which is a project of the Jet Propulsion Laboratory/California Institute of Technology, funded by the Planetary Science Division of the National Aeronautics and Space Administration. This work is supported by the National Key R&D Program of China (2021YFA0718500) and the National Natural Science Foundation of China (Grants No. U2031205, 11733009). X. Wang is supported by the National Science Foundation of China (NSFC grants 12033003 and 11633002), the Scholar Program of Beijing Academy of Science and Technology (DZ:BS202002), and the Tencent Explorer Prize.

References

- Bikmaev, I., Shimansky, V., Irtuganov, E., et al. 2017, *The Astronomer's Telegram*, 10968
- Carciofi, A. C. 2011, *Active OB Stars: Structure, Evolution, Mass Loss, and Critical Limits*, 272, 325. doi:10.1017/S1743921311010738
- Doroshenko, V., Tsygankov, S., & Santangelo, A. 2018, *A&A*, 613, A19. doi:10.1051/0004-6361/201732208
- Doroshenko, V., Zhang, S. N., Santangelo, A., et al. 2020, *MNRAS*, 491, 1857. doi:10.1093/mnras/stz2879
- Gaia Collaboration 2022, *VizieR Online Data Catalog*, I/355
- Gaia Collaboration, Prusti, T., de Bruijne, J. H. J., et al. 2016, *A&A*, 595, A1. doi:10.1051/0004-6361/201629272
- Hanuschik, R. W., Hummel, W., Dietle, O., et al. 1995, *A&A*, 300, 163
- Harmanec, P. 1983, *Hvar Observatory Bulletin*, 7, 55
- Hayasaki, K. & Okazaki, A. T. 2004, astro-ph/0412203, Conference Proceeding for the "Interacting Binaries: Accretion, Evolution and Outcome" workshop held in Cefalu' (Italy), July 2004
- Huang, F., Li, J.-Z., Wang, X.-F., et al. 2012, *Research in Astronomy and Astrophysics*, 12, 1585. doi:10.1088/1674-4527/12/11/012
- Jayasinghe, T., Stanek, K. Z., Kochanek, C. S., et al. 2019, *MNRAS*, 486, 1907. doi:10.1093/mnras/stz844
- Jenke, P. & Wilson-Hodge, C. A. 2017, *The Astronomer's Telegram*, 10812
- Kennea, J. A., Lien, A. Y., Krimm, H. A., et al. 2017, *The Astronomer's Telegram*, 10809
- Kong, L.-D., Zhang, S., Zhang, S.-N., et al. 2022, arXiv:2206.04283
- Krimm, H. A., Holland, S. T., Corbet, R. H. D., et al. 2013, *ApJS*, 209, 14. doi:10.1088/0067-0049/209/1/14
- Liu, Q. Z., van Paradijs, J., & van den Heuvel, E. P. J. 2006, *A&A*, 455, 1165. doi:10.1051/0004-6361:20064987
- Mainzer, A., Bauer, J., Grav, T., et al. 2011, *ApJ*, 731, 53. doi:10.1088/0004-637X/731/1/53
- Meegan, C., Lichti, G., Bhat, P. N., et al. 2009, *ApJ*, 702, 791. doi:10.1088/0004-637X/702/1/791
- Mennickent, R. E., Sterken, C., & Vogt, N. 1997, *A&A*, 326, 1167
- Negueruela, I., Steele, I. A., & Bernabeu, G. 2004, *Astronomische Nachrichten*, 325, 749. doi:10.1002/asna.200310258
- Nesci, R. 2017, *The Astronomer's Telegram*, 10989
- Okazaki, A. T. 1997, *A&A*, 318, 548
- Reig, P. 2011, *Ap&SS*, 332, 1. doi:10.1007/s10509-010-0575-8
- Reig, P. & Roche, P. 1999, *MNRAS*, 306, 100. doi:10.1046/j.1365-8711.1999.02473.x
- Reig, P., Nersesian, A., Zezas, A., et al. 2016, *A&A*, 590, A122. doi:10.1051/0004-6361/201628271
- Reig, P., Fabregat, J., & Alfonso-Garzón, J. 2020, *A&A*, 640, A35. doi:10.1051/0004-6361/202038333
- Rivinius, Thomas, Carciofi, Alex C., and Martayan, Christophe, 2013, *The Astronomy and Astrophysics Review*, 21, 69
- Shappee, B. J., Prieto, J. L., Grupe, D., et al. 2014, *ApJ*, 788, 48. doi:10.1088/0004-637X/788/1/48
- Slettebak, A., Collins, G. W., & Truax, R. 1992, *ApJS*, 81, 335. doi:10.1086/191696
- Telting, J. H., Heemskerk, M. H. M., Henrichs, H. F., et al. 1994, *A&A*, 288, 558
- Tsygankov, S. S., Doroshenko, V., Mushtukov, A. A., et al. 2018, *MNRAS*, 479, L134. doi:10.1093/mnras/sly116
- van den Ejijnden, J., Degenaar, N., Russell, T. D., et al. 2018, *Nature*, 562, 233. doi:10.1038/s41586-018-0524-1
- Wang, X., Li, W., Filippenko, A. V., et al. 2008, *ApJ*, 675, 626. doi:10.1086/526413
- Zhang, Y., Ge, M., Song, L., et al. 2019, *ApJ*, 879, 61. doi:10.3847/1538-4357/ab22b1
- Ziolkowski, J. 2002, *Mem. Soc. Astron. Italiana*, 73, 1038

Appendix A: Table of spectroscopic observations

Appendix B: Table of V / R ratio and peak separation

Appendix C: Table of photometric observations

Table A.1. Spectroscopic observations of Swift J0243.6+6124 between 2017 and 2021.

Date (DD-MM-YYYY)	MJD	Telescope/ Instrument	Wavelength Range (Å)	EW(H α) (Å)	EW(He I λ 6678) (Å)
04-10-2017	58030.8342	2.16 m/BFOSC	4000-8700	-10.6 \pm 0.2	...
13-10-2017	58039.6745	2.16 m/BFOSC	4000-8700	-10.1 \pm 0.1	...
27-10-2017	58053.6744	2.16 m/OMR	5500-6900	-8.5 \pm 0.1	-0.39 \pm 0.08
27-10-2017	58053.8025	2.16 m/OMR	5500-6900	-8.0 \pm 0.4	-0.41 \pm 0.11
28-10-2017	58054.6191	2.16 m/OMR	5500-6900	-8.7 \pm 0.4	-0.32 \pm 0.12
29-10-2017	58055.6853	2.16 m/OMR	5500-6900	-9.4 \pm 0.3	-0.31 \pm 0.16
11-11-2017	58068.6412	2.16 m/OMR	5500-6900	-10.3 \pm 0.6	-0.28 \pm 0.23
11-11-2017	58068.7547	2.16 m/OMR	5500-6900	-10.6 \pm 0.2	-0.52 \pm 0.12
12-11-2017	58069.7245	2.16 m/OMR	5500-6900	-11.0 \pm 0.5	-0.42 \pm 0.09
13-11-2017	58070.7783	2.16 m/BFOSC	4000-8700	-11.2 \pm 0.2	...
23-11-2017	58080.5667	2.4 m/YFOSC	4970-9830	-10.0 \pm 0.2	-0.23 \pm 0.06
23-11-2017	58080.6792	2.4 m/YFOSC	4970-9830	-10.0 \pm 0.2	-0.22 \pm 0.06
24-11-2017	58081.5326	2.4 m/YFOSC	4970-9830	-9.6 \pm 0.2	-0.27 \pm 0.06
25-11-2017	58082.5549	2.4 m/YFOSC	4970-9830	-9.9 \pm 0.1	-0.22 \pm 0.03
07-01-2018	58125.6306	2.4 m/YFOSC	4970-9830	-10.7 \pm 0.1	-0.25 \pm 0.09
08-01-2018	58126.5597	2.4 m/YFOSC	3700-7630	-10.6 \pm 0.2	-0.30 \pm 0.06
10-01-2018	58128.5208	2.16 m/BFOSC	4000-8700	-10.3 \pm 0.4	...
23-01-2018	58141.5189	2.16 m/BFOSC	4000-8700	-11.2 \pm 0.1	...
24-01-2018	58142.5440	2.16 m/BFOSC	4000-8700	-11.7 \pm 0.1	...
12-02-2018	58160.4380	2.16 m/BFOSC	4000-8700	-10.8 \pm 0.1	...
19-02-2018	58168.4470	2.16 m/BFOSC	4000-8700	-10.8 \pm 0.2	...
25-03-2018	58202.4619	2.16 m/BFOSC	4000-8700	-10.7 \pm 0.3	...
17-09-2018	58378.7433	2.16 m/OMR	5500-6900	-8.2 \pm 0.5	-0.30 \pm 0.03
23-09-2018	58384.7466	2.16 m/BFOSC	4000-8700	-9.0 \pm 0.1	...
03-10-2018	58394.8377	2.16 m/BFOSC	4000-8700	-9.4 \pm 0.1	...
15-11-2018	58437.6707	2.16 m/BFOSC	4000-8700	-7.3 \pm 0.6	...
17-11-2018	58439.6922	2.16 m/BFOSC	4000-8700	-7.5 \pm 0.2	...
21-11-2018	58443.5873	2.16 m/BFOSC	4000-8700	-7.6 \pm 0.0	...
22-11-2018	58444.6232	2.16 m/BFOSC	4000-8700	-7.4 \pm 0.2	...
27-11-2018	58449.6591	2.16 m/BFOSC	4000-8700	-8.1 \pm 0.1	...
04-12-2018	58455.7521	2.16 m/BFOSC	4000-8700	-7.4 \pm 0.7	...
25-12-2018	58477.5579	2.4 m/YFOSC	4970-9830	-6.8 \pm 0.1	-0.12 \pm 0.06
26-12-2018	58478.5499	2.4 m/YFOSC	4970-9830	-6.9 \pm 0.2	-0.13 \pm 0.06
27-12-2018	58479.5959	2.4 m/YFOSC	4970-9830	-7.0 \pm 0.2	-0.13 \pm 0.05
28-12-2018	58480.5463	2.4 m/YFOSC	4970-9830	-7.2 \pm 0.2	-0.20 \pm 0.08
09-01-2019	58492.6229	2.16 m/BFOSC	4000-8700	-7.2 \pm 0.2	...
27-01-2019	58510.5146	2.16 m/BFOSC	5200-8200	-7.3 \pm 0.1	...
27-01-2019	58510.5481	2.4 m/YFOSC	3500-8750	-7.0 \pm 0.1	-0.18 \pm 0.07
09-02-2019	58523.4430	2.16 m/BFOSC	4400-8700	-6.6 \pm 0.4	...
07-10-2019	58763.8718	2.16 m/BFOSC	4000-8700	-5.5 \pm 0.3	...
03-11-2019	58790.7485	2.16 m/OMR	5500-6900	-5.2 \pm 0.4	-0.04 \pm 0.03
04-11-2019	58792.2656	2.16 m/OMR	5500-6900	-5.3 \pm 0.3	0.01 \pm 0.04
26-12-2019	58843.6260	2.4 m/YFOSC	4970-9830	-6.0 \pm 0.2	0.06 \pm 0.03
21-07-2020	59052.0035	SKO/1.3 m	5400-7300	-6.8 \pm 0.1	-0.01 \pm 0.02
20-08-2020	59082.0787	SKO/1.3 m	5400-7300	-6.7 \pm 0.0	-0.01 \pm 0.06
14-09-2020	59107.0080	SKO/1.3 m	5400-7300	-7.3 \pm 0.1	...
16-09-2020	59108.9829	SKO/1.3 m	5400-7300	-6.7 \pm 0.0	-0.03 \pm 0.05
29-09-2020	59122.0820	SKO/1.3 m	5400-7300	-5.7 \pm 0.1	0.08 \pm 0.04
10-10-2020	59132.6655	2.16 m/BFOSC	5800-8280	-6.8 \pm 0.2	0.01 \pm 0.05
11-10-2020	59133.8369	2.16 m/BFOSC	5800-8280	-7.1 \pm 0.1	0.07 \pm 0.02
12-10-2020	59134.7450	2.16 m/BFOSC	5800-8280	-7.0 \pm 0.1	-0.01 \pm 0.04
11-08-2021	59437.9970	SKO/1.3 m	5400-7300	-8.0 \pm 0.1	-0.07 \pm 0.04
01-09-2021	59459.0720	SKO/1.3 m	5400-7300	-8.3 \pm 0.0	-0.06 \pm 0.03
05-09-2021	59463.0289	SKO/1.3 m	5400-7300	-8.2 \pm 0.1	-0.09 \pm 0.04
09-10-2021	59496.9755	SKO/1.3 m	5400-7300	-8.2 \pm 0.1	-0.07 \pm 0.05
10-10-2021	59497.6557	2.16 m/OMR	6000-6850	-8.4 \pm 0.1	-0.11 \pm 0.06

Table B.1. V/R ratio and peak separation of Swift J0243.6+6124 between 2017 and 2021.

Date (DD-MM-YYYY)	MJD	Telescope/ Instrument	Wavelength Range (Å)	$\log(V/R)(H\alpha)$	$\Delta V(H\alpha)$ (km s^{-1})
27-10-2017	58053.6744	2.16 m/OMR	5500-6900	0.453	230
27-10-2017	58053.8025	2.16 m/OMR	5500-6900	0.495	211
28-10-2017	58054.6191	2.16 m/OMR	5500-6900	0.537	217
29-10-2017	58055.6853	2.16 m/OMR	5500-6900	0.462	228
11-11-2017	58068.6412	2.16 m/OMR	5500-6900	0.390	195
11-11-2017	58068.7547	2.16 m/OMR	5500-6900	0.404	195
12-11-2017	58069.7245	2.16 m/OMR	5500-6900	0.516	197
17-09-2018	58378.7433	2.16 m/OMR	5500-6900	0.603	222
15-11-2018	58437.6707	2.16 m/BFOSC	4000-8700	-0.042	...
25-12-2018	58477.5579	2.4 m/YFOSC	4970-9830	-0.406	232
03-11-2019	58790.7485	2.16 m/OMR	5500-6900	-0.193	212
04-11-2019	58792.2656	2.16 m/OMR	5500-6900	-0.168	185
20-08-2020	59082.0787	SKO/1.3 m	5400-7300	0.022	140
09-10-2021	59496.9755	SKO/1.3 m	5400-7300	0.314	218
10-10-2021	59497.6557	2.16 m/OMR	6000-6850	0.198	207

Table C.1. Photometric observations of Swift J0243.6+6124 between 2017 and 2022.

MJD	Telescope	<i>B</i> (mag)	<i>V</i> (mag)	<i>R</i> (mag)	<i>I</i> (mag)
58038.62	60cm	13.725 ± 0.010	12.777 ± 0.010	12.065 ± 0.010	11.241 ± 0.020
58039.81	60cm	13.704 ± 0.010	12.729 ± 0.010	12.030 ± 0.010	11.206 ± 0.020
58041.76	60cm	13.652 ± 0.010	12.720 ± 0.010	12.014 ± 0.010	11.176 ± 0.020
58042.72	60cm	13.700 ± 0.010	12.755 ± 0.010	12.046 ± 0.010	11.234 ± 0.020
58045.72	60cm	13.724 ± 0.010	12.768 ± 0.010	12.066 ± 0.010	11.216 ± 0.020
58046.63	60cm	13.710 ± 0.010	12.757 ± 0.010	12.036 ± 0.010	11.198 ± 0.020
58049.86	60cm	13.681 ± 0.010	12.680 ± 0.010	12.232 ± 0.010	11.152 ± 0.020
58052.78	60cm	13.582 ± 0.010	12.632 ± 0.010	11.963 ± 0.010	11.093 ± 0.020
58053.70	80cm	13.644 ± 0.010	12.702 ± 0.010	11.974 ± 0.010	11.156 ± 0.020
58053.77	60cm	13.636 ± 0.010	12.687 ± 0.010	11.944 ± 0.010	11.131 ± 0.020
58054.63	60cm	13.405 ± 0.010	12.476 ± 0.010	11.861 ± 0.010	11.058 ± 0.020
58054.70	80cm	13.543 ± 0.010	12.639 ± 0.011	11.942 ± 0.011	11.137 ± 0.021
58055.64	60cm	13.617 ± 0.010	12.671 ± 0.010	11.963 ± 0.010	11.155 ± 0.020
58055.70	80cm	13.631 ± 0.010	12.683 ± 0.010	11.961 ± 0.011	11.140 ± 0.020
58056.62	60cm	13.626 ± 0.010	12.680 ± 0.010	11.977 ± 0.010	11.160 ± 0.020
58056.74	80cm	13.629 ± 0.010	12.681 ± 0.011	11.952 ± 0.011	11.126 ± 0.020
58059.78	60cm	13.233 ± 0.010	12.361 ± 0.010	11.694 ± 0.010	10.949 ± 0.020
58061.71	80cm	13.465 ± 0.017	12.577 ± 0.015	11.874 ± 0.013	11.038 ± 0.022
58061.80	60cm	13.443 ± 0.010	12.491 ± 0.010	11.767 ± 0.010	10.956 ± 0.020
58062.65	80cm	13.547 ± 0.014	12.600 ± 0.013	11.857 ± 0.012	11.028 ± 0.021
58063.56	80cm	13.433 ± 0.027	12.537 ± 0.023	11.801 ± 0.019	10.992 ± 0.024
58064.65	80cm	13.483 ± 0.011	12.556 ± 0.011	11.838 ± 0.011	11.007 ± 0.020
58065.69	80cm	13.541 ± 0.012	12.574 ± 0.012	11.846 ± 0.012	11.019 ± 0.021
58067.57	60cm	13.398 ± 0.010	12.471 ± 0.010	11.804 ± 0.010	10.975 ± 0.020
58069.57	60cm	13.504 ± 0.010	12.554 ± 0.010	11.849 ± 0.010	11.008 ± 0.020
58073.52	60cm	13.571 ± 0.010	12.613 ± 0.010	11.890 ± 0.010	11.078 ± 0.020
58074.65	80cm	13.440 ± 0.010	12.518 ± 0.011	11.814 ± 0.011	10.990 ± 0.021
58080.61	2.4m	13.628 ± 0.010	12.663 ± 0.010	11.932 ± 0.010	11.102 ± 0.020
58081.53	2.4m	13.638 ± 0.010	12.677 ± 0.010	11.943 ± 0.010	11.103 ± 0.020
58082.55	2.4m	13.649 ± 0.010	12.681 ± 0.010	11.942 ± 0.010	11.122 ± 0.020
58083.60	60cm	13.540 ± 0.010	12.623 ± 0.010	11.913 ± 0.010	11.096 ± 0.020
58086.62	60cm	13.572 ± 0.010	12.630 ± 0.010	11.872 ± 0.010	11.142 ± 0.020
58088.56	60cm	13.591 ± 0.010	12.643 ± 0.010	11.931 ± 0.010	11.129 ± 0.020
58095.62	60cm	13.661 ± 0.010	12.716 ± 0.010	12.002 ± 0.010	11.187 ± 0.020
58117.58	80cm	13.700 ± 0.011	12.762 ± 0.011	12.103 ± 0.011	11.215 ± 0.020
58118.57	80cm	13.720 ± 0.011	12.774 ± 0.011	12.040 ± 0.011	11.218 ± 0.020
58123.64	60cm	13.733 ± 0.010	12.800 ± 0.010	12.099 ± 0.010	11.296 ± 0.020
58125.64	2.4m	13.735 ± 0.010	12.783 ± 0.010	12.047 ± 0.011	11.242 ± 0.020
58126.56	2.4m	13.699 ± 0.010	12.772 ± 0.010	12.068 ± 0.010	11.235 ± 0.020
58135.60	60cm	13.751 ± 0.010	12.805 ± 0.010	12.097 ± 0.010	11.285 ± 0.020
58138.57	60cm	13.488 ± 0.010	12.770 ± 0.010	12.064 ± 0.010	11.119 ± 0.020
58148.53	60cm	13.724 ± 0.010	12.794 ± 0.010	12.079 ± 0.010	11.298 ± 0.020
58150.51	60cm	13.739 ± 0.010	12.786 ± 0.010	12.088 ± 0.010	11.283 ± 0.020
58152.52	60cm	13.625 ± 0.010	12.825 ± 0.010	12.145 ± 0.010	...
58153.52	60cm	13.732 ± 0.010	12.812 ± 0.010	12.128 ± 0.010	11.320 ± 0.020
58156.43	60cm	13.690 ± 0.010	12.803 ± 0.010	12.081 ± 0.010	11.277 ± 0.020
58158.44	60cm	13.733 ± 0.010	12.788 ± 0.010	12.085 ± 0.010	11.264 ± 0.020
58161.47	60cm	13.751 ± 0.010	12.758 ± 0.010	12.044 ± 0.010	11.219 ± 0.020
58171.47	60cm	13.792 ± 0.010	12.845 ± 0.010	12.116 ± 0.010	11.340 ± 0.020
58173.49	60cm	13.719 ± 0.010	12.792 ± 0.010	12.103 ± 0.010	11.290 ± 0.020
58175.47	60cm	13.756 ± 0.010	12.815 ± 0.010	12.128 ± 0.010	11.325 ± 0.020
58178.47	60cm	13.735 ± 0.010	12.847 ± 0.010	12.149 ± 0.010	11.337 ± 0.020
58179.46	60cm	13.698 ± 0.010	12.780 ± 0.010	12.111 ± 0.010	11.346 ± 0.020
58185.46	60cm	13.779 ± 0.010	12.843 ± 0.010	12.125 ± 0.010	11.323 ± 0.020
58186.46	60cm	13.626 ± 0.010	12.763 ± 0.010	12.052 ± 0.010	11.250 ± 0.020
58187.47	60cm	13.712 ± 0.010	12.769 ± 0.010	12.114 ± 0.010	11.312 ± 0.020
58192.46	60cm	13.727 ± 0.010	12.794 ± 0.010	12.067 ± 0.010	11.296 ± 0.020
58200.46	60cm	13.780 ± 0.010	12.844 ± 0.010	12.135 ± 0.010	11.315 ± 0.020
58201.49	60cm	13.805 ± 0.010	12.873 ± 0.010	12.184 ± 0.010	11.381 ± 0.020
58202.48	60cm	13.771 ± 0.010	12.836 ± 0.010	12.158 ± 0.010	11.372 ± 0.020

Table C.1. continued.

MJD	Telescope	<i>B</i> (mag)	<i>V</i> (mag)	<i>R</i> (mag)	<i>I</i> (mag)
58203.49	60cm	13.675 ± 0.012	12.757 ± 0.011	12.081 ± 0.010	11.293 ± 0.020
58216.47	60cm	13.790 ± 0.011	12.851 ± 0.010	12.136 ± 0.010	11.355 ± 0.020
58218.48	60cm	13.738 ± 0.010	12.844 ± 0.010	12.088 ± 0.010	11.365 ± 0.020
58219.48	60cm	13.780 ± 0.010	12.860 ± 0.010	12.137 ± 0.010	11.376 ± 0.020
58368.74	60cm	13.863 ± 0.010	12.899 ± 0.010	12.275 ± 0.010	11.540 ± 0.020
58369.76	80cm	13.827 ± 0.012	12.920 ± 0.011	12.059 ± 0.010	11.504 ± 0.021
58370.78	60cm	13.806 ± 0.010	12.905 ± 0.010	12.238 ± 0.010	11.474 ± 0.020
58377.75	80cm	13.859 ± 0.011	12.940 ± 0.010	12.259 ± 0.011	11.498 ± 0.020
58378.79	80cm	13.854 ± 0.011	12.935 ± 0.010	12.273 ± 0.010	11.481 ± 0.020
58382.83	60cm	13.849 ± 0.010	12.926 ± 0.010	12.280 ± 0.010	11.496 ± 0.020
58383.78	60cm	13.853 ± 0.010	12.941 ± 0.010	12.295 ± 0.010	11.501 ± 0.020
58385.75	60cm	13.803 ± 0.010	12.873 ± 0.010	12.206 ± 0.010	11.510 ± 0.020
58397.71	60cm	13.860 ± 0.010	12.960 ± 0.010	12.310 ± 0.010	11.529 ± 0.020
58398.80	60cm	13.855 ± 0.010	12.930 ± 0.010	12.332 ± 0.010	11.552 ± 0.020
58408.80	60cm	13.887 ± 0.010	12.963 ± 0.010	12.285 ± 0.010	11.519 ± 0.020
58409.79	60cm	13.873 ± 0.010	12.945 ± 0.010	12.297 ± 0.010	11.527 ± 0.020
58410.72	60cm	13.886 ± 0.010	12.971 ± 0.010	12.282 ± 0.010	11.514 ± 0.020
58411.67	60cm	13.812 ± 0.010	12.922 ± 0.010	12.268 ± 0.010	11.494 ± 0.020
58414.58	60cm	13.850 ± 0.010	12.951 ± 0.010	12.293 ± 0.010	11.530 ± 0.020
58421.69	60cm	13.887 ± 0.010	12.969 ± 0.010	12.294 ± 0.010	11.520 ± 0.020
58422.67	60cm	13.919 ± 0.010	12.970 ± 0.010	12.300 ± 0.010	11.525 ± 0.020
58425.63	60cm	13.858 ± 0.010	12.977 ± 0.010	12.323 ± 0.010	11.549 ± 0.020
58428.75	80cm	13.855 ± 0.011	12.967 ± 0.010	12.268 ± 0.010	11.557 ± 0.020
58430.68	80cm	13.883 ± 0.011	12.978 ± 0.010	12.313 ± 0.010	11.564 ± 0.020
58456.62	80cm	13.896 ± 0.011	12.993 ± 0.010	12.324 ± 0.011	11.581 ± 0.021
58468.53	60cm	13.902 ± 0.010	12.996 ± 0.010	12.334 ± 0.010	11.570 ± 0.020
58469.59	60cm	13.896 ± 0.010	12.973 ± 0.010	12.342 ± 0.010	11.571 ± 0.020
58476.54	60cm	13.814 ± 0.010	12.921 ± 0.010	12.276 ± 0.010	11.512 ± 0.020
58477.53	60cm	13.835 ± 0.010	12.943 ± 0.010	12.285 ± 0.010	11.525 ± 0.020
58477.55	2.4m	13.864 ± 0.010	12.963 ± 0.010	12.339 ± 0.010	11.532 ± 0.020
58478.54	60cm	13.844 ± 0.010	12.938 ± 0.010	12.275 ± 0.010	11.523 ± 0.020
58478.55	2.4m	13.881 ± 0.010	12.971 ± 0.010	12.301 ± 0.010	11.543 ± 0.020
58479.60	2.4m	13.884 ± 0.010	12.975 ± 0.010	12.304 ± 0.010	11.548 ± 0.020
58480.54	2.4m	13.887 ± 0.010	12.970 ± 0.010	12.306 ± 0.010	11.541 ± 0.020
58481.55	60cm	13.806 ± 0.010	12.938 ± 0.010	12.316 ± 0.010	11.516 ± 0.020
58482.55	60cm	13.890 ± 0.010	12.982 ± 0.010	12.330 ± 0.010	11.554 ± 0.020
58484.53	60cm	13.885 ± 0.010	12.974 ± 0.010	12.320 ± 0.010	11.554 ± 0.020
58485.54	60cm	13.876 ± 0.010	12.960 ± 0.010	12.296 ± 0.010	11.538 ± 0.020
58487.53	60cm	13.806 ± 0.010	12.894 ± 0.010	12.296 ± 0.010	11.520 ± 0.020
58489.58	60cm	13.881 ± 0.010	12.965 ± 0.010	12.303 ± 0.010	11.506 ± 0.020
58490.63	60cm	13.797 ± 0.010	12.881 ± 0.010	12.278 ± 0.010	11.498 ± 0.020
58491.52	60cm	13.846 ± 0.010	12.965 ± 0.010	12.306 ± 0.010	11.533 ± 0.020
58499.49	60cm	13.822 ± 0.010	12.925 ± 0.010	12.287 ± 0.010	11.517 ± 0.020
58500.46	60cm	13.847 ± 0.010	12.977 ± 0.010	12.302 ± 0.010	11.557 ± 0.020
58501.48	60cm	13.852 ± 0.010	12.951 ± 0.010	12.261 ± 0.010	11.527 ± 0.020
58504.47	60cm	13.869 ± 0.010	12.955 ± 0.010	12.313 ± 0.010	11.556 ± 0.020
58509.44	60cm	13.899 ± 0.010	12.990 ± 0.010	12.318 ± 0.010	11.567 ± 0.020
58510.45	60cm	13.905 ± 0.010	13.006 ± 0.010	12.348 ± 0.010	11.561 ± 0.020
58510.54	2.16m	13.844 ± 0.010	12.945 ± 0.010	12.301 ± 0.010	11.534 ± 0.020
58511.46	60cm	13.904 ± 0.010	12.994 ± 0.010	12.360 ± 0.010	11.584 ± 0.020
58514.47	60cm	13.850 ± 0.010	12.957 ± 0.010	12.281 ± 0.010	11.545 ± 0.020
58515.45	60cm	13.908 ± 0.010	12.998 ± 0.010	12.370 ± 0.010	11.565 ± 0.020
58525.45	60cm	13.826 ± 0.010	12.909 ± 0.010	12.275 ± 0.010	11.538 ± 0.020
58534.47	60cm	13.886 ± 0.010	12.997 ± 0.010	...	11.597 ± 0.020
58537.45	60cm	13.872 ± 0.010	12.963 ± 0.010	12.315 ± 0.010	11.564 ± 0.020
58538.52	60cm	13.899 ± 0.010	12.952 ± 0.010	12.318 ± 0.010	11.558 ± 0.020
58728.83	60cm	13.835 ± 0.010	12.893 ± 0.010	12.233 ± 0.010	...
58731.83	60cm	13.846 ± 0.010	12.926 ± 0.010	12.263 ± 0.010	11.491 ± 0.020
58732.77	60cm	13.838 ± 0.010	12.911 ± 0.010	12.246 ± 0.010	11.481 ± 0.020
58733.87	60cm	13.765 ± 0.011	12.852 ± 0.010	12.253 ± 0.010	11.431 ± 0.020

Table C.1. continued.

MJD	Telescope	<i>B</i> (mag)	<i>V</i> (mag)	<i>R</i> (mag)	<i>I</i> (mag)
58743.73	60cm	13.815 ± 0.010	12.915 ± 0.010	12.254 ± 0.010	11.471 ± 0.020
58744.74	60cm	13.780 ± 0.010	12.873 ± 0.010	12.193 ± 0.010	...
58749.67	60cm	13.828 ± 0.010	12.911 ± 0.010	12.237 ± 0.010	11.445 ± 0.020
58750.75	80cm	13.812 ± 0.011	12.898 ± 0.010	12.312 ± 0.010	11.461 ± 0.020
58751.76	80cm	13.862 ± 0.011	12.937 ± 0.010	12.255 ± 0.010	11.495 ± 0.020
58752.67	60cm	13.829 ± 0.010	12.899 ± 0.010	12.247 ± 0.010	11.442 ± 0.020
58757.61	60cm	13.777 ± 0.010	12.870 ± 0.010	12.209 ± 0.010	11.424 ± 0.020
58764.59	60cm	13.776 ± 0.010	12.832 ± 0.010	12.216 ± 0.010	11.379 ± 0.020
58776.64	60cm	13.756 ± 0.010	12.824 ± 0.010	12.108 ± 0.010	11.418 ± 0.020
58777.69	60cm	13.820 ± 0.010	12.886 ± 0.010	12.229 ± 0.010	11.443 ± 0.020
58782.70	60cm	13.820 ± 0.010	12.868 ± 0.010	12.184 ± 0.010	11.421 ± 0.020
58785.71	60cm	13.742 ± 0.010	12.846 ± 0.010	12.187 ± 0.010	11.424 ± 0.020
58786.68	60cm	13.780 ± 0.010	12.884 ± 0.010	12.201 ± 0.010	11.453 ± 0.020
58787.68	60cm	13.835 ± 0.010	12.903 ± 0.010	12.224 ± 0.010	11.455 ± 0.020
58790.59	60cm	13.774 ± 0.010	12.858 ± 0.010	12.191 ± 0.010	11.388 ± 0.020
58790.63	80cm	13.798 ± 0.011	12.871 ± 0.011	12.122 ± 0.010	11.437 ± 0.020
58791.66	80cm	13.798 ± 0.011	12.876 ± 0.010	12.209 ± 0.011	11.441 ± 0.020
58792.63	60cm	13.748 ± 0.010	12.827 ± 0.010	12.170 ± 0.010	11.392 ± 0.020
58793.63	60cm	13.762 ± 0.010	12.872 ± 0.010	12.200 ± 0.010	11.465 ± 0.020
58793.83	80cm	13.731 ± 0.011	12.809 ± 0.011	12.215 ± 0.010	11.436 ± 0.021
58794.63	60cm	13.736 ± 0.010	12.842 ± 0.010	12.214 ± 0.010	11.394 ± 0.020
58805.61	60cm	13.724 ± 0.010	12.855 ± 0.010	12.171 ± 0.010	11.429 ± 0.020
58806.61	60cm	13.821 ± 0.010	12.899 ± 0.010	12.227 ± 0.010	11.446 ± 0.020
58807.67	60cm	13.782 ± 0.011	12.825 ± 0.010	12.185 ± 0.010	11.405 ± 0.020
58843.64	2.4m	13.800 ± 0.010	12.877 ± 0.010	12.171 ± 0.011	11.397 ± 0.020
58852.50	60cm	13.818 ± 0.010	12.902 ± 0.010	12.226 ± 0.010	11.429 ± 0.020
59098.77	80cm	13.771 ± 0.012	12.829 ± 0.011	12.190 ± 0.010	11.339 ± 0.021
59099.79	80cm	13.766 ± 0.011	12.828 ± 0.011	12.134 ± 0.011	11.339 ± 0.020
59100.68	80cm	13.767 ± 0.011	12.828 ± 0.011	12.125 ± 0.011	11.342 ± 0.020
59101.70	80cm	13.768 ± 0.011	12.822 ± 0.011	12.140 ± 0.011	11.336 ± 0.020
59107.75	80cm	13.735 ± 0.011	12.800 ± 0.011	12.134 ± 0.011	11.331 ± 0.020
59108.74	80cm	13.697 ± 0.011	12.772 ± 0.010	12.130 ± 0.011	11.317 ± 0.020
59109.75	80cm	13.756 ± 0.011	12.813 ± 0.010	12.125 ± 0.011	11.322 ± 0.020
59131.71	80cm	13.762 ± 0.014	12.814 ± 0.013	12.122 ± 0.012	11.325 ± 0.022
59133.74	80cm	13.730 ± 0.011	12.797 ± 0.010	12.117 ± 0.011	11.313 ± 0.020
59134.76	80cm	13.756 ± 0.011	12.816 ± 0.011	12.127 ± 0.011	11.324 ± 0.020
59497.78	80cm	13.743 ± 0.011	12.803 ± 0.011	12.104 ± 0.011	11.308 ± 0.020
59564.53	80cm'	13.801 ± 0.010	12.812 ± 0.010	12.117 ± 0.010	11.351 ± 0.020
59565.51	80cm'	13.797 ± 0.011	12.801 ± 0.010	12.114 ± 0.010	11.345 ± 0.020
59567.51	80cm'	13.800 ± 0.010	12.804 ± 0.010	12.111 ± 0.010	11.346 ± 0.020
59568.53	80cm'	13.791 ± 0.010	12.793 ± 0.010	12.100 ± 0.010	11.337 ± 0.020
59569.57	80cm'	13.780 ± 0.010	12.799 ± 0.010	12.103 ± 0.010	11.341 ± 0.020
59570.54	80cm'	13.797 ± 0.010	12.803 ± 0.010	12.113 ± 0.010	11.350 ± 0.020
59571.50	80cm'	13.796 ± 0.010	12.809 ± 0.011	12.098 ± 0.014	11.348 ± 0.020
59572.51	80cm'	13.799 ± 0.010	12.805 ± 0.010	12.107 ± 0.010	11.359 ± 0.020
59573.71	80cm'	13.771 ± 0.019	12.798 ± 0.013	12.106 ± 0.013	...
59576.64	80cm'	13.803 ± 0.010	12.798 ± 0.010	12.104 ± 0.010	11.333 ± 0.020
59577.63	80cm'	13.794 ± 0.010	12.800 ± 0.010	12.106 ± 0.010	11.345 ± 0.020
59578.60	80cm'	13.799 ± 0.010	12.799 ± 0.010	12.103 ± 0.010	11.343 ± 0.020
59579.63	80cm'	13.797 ± 0.010	12.801 ± 0.010	12.114 ± 0.010	11.342 ± 0.020
59580.67	80cm'	13.797 ± 0.010	12.799 ± 0.010	12.103 ± 0.010	11.337 ± 0.020
59581.67	80cm'	13.784 ± 0.010	12.799 ± 0.010	12.106 ± 0.010	11.339 ± 0.020
59582.62	80cm'	13.797 ± 0.010	12.805 ± 0.010	12.113 ± 0.010	11.345 ± 0.020
59583.63	80cm'	13.794 ± 0.010	12.795 ± 0.010	12.107 ± 0.010	11.347 ± 0.020
59584.62	80cm'	13.795 ± 0.010	12.804 ± 0.010	12.110 ± 0.010	11.356 ± 0.020
59586.61	80cm'	13.799 ± 0.010	12.807 ± 0.010	12.116 ± 0.010	11.357 ± 0.020
59587.60	80cm'	13.798 ± 0.010	12.805 ± 0.010	12.118 ± 0.010	11.356 ± 0.020
59588.60	80cm'	13.797 ± 0.010	12.806 ± 0.010	12.113 ± 0.010	11.350 ± 0.020
59589.61	80cm'	13.793 ± 0.010	12.797 ± 0.010	12.118 ± 0.010	11.352 ± 0.020
59590.59	80cm'	13.806 ± 0.010	12.809 ± 0.010	12.119 ± 0.010	11.349 ± 0.020

Table C.1. continued.

MJD	Telescope	<i>B</i> (mag)	<i>V</i> (mag)	<i>R</i> (mag)	<i>I</i> (mag)
59591.63	80cm'	13.804 ± 0.010	12.802 ± 0.010	12.109 ± 0.010	11.346 ± 0.020
59608.67	80cm'	13.773 ± 0.010	12.794 ± 0.010	12.113 ± 0.010	11.347 ± 0.020
59612.66	80cm'	13.736 ± 0.011	12.776 ± 0.010	12.094 ± 0.010	11.341 ± 0.020
59617.61	80cm'	13.809 ± 0.010	12.810 ± 0.010	12.121 ± 0.010	11.358 ± 0.020
59621.64	80cm'	13.788 ± 0.015	...	12.089 ± 0.011	11.328 ± 0.054
59625.63	80cm'	13.787 ± 0.011	12.791 ± 0.010	12.095 ± 0.010	11.333 ± 0.020
59634.60	80cm'	13.786 ± 0.011	12.792 ± 0.010	12.091 ± 0.010	11.323 ± 0.020
59638.59	80cm'	13.789 ± 0.010	12.798 ± 0.010	12.116 ± 0.010	11.349 ± 0.020
59642.57	80cm'	13.793 ± 0.010	12.803 ± 0.010	12.104 ± 0.010	11.343 ± 0.020
59646.57	80cm'	13.784 ± 0.011	12.781 ± 0.010	12.104 ± 0.010	11.347 ± 0.020
59650.56	80cm'	13.784 ± 0.013	12.794 ± 0.011	12.109 ± 0.013	11.337 ± 0.022
59654.55	80cm'	13.778 ± 0.019	12.800 ± 0.012	12.086 ± 0.012	11.337 ± 0.021
59658.54	80cm'	13.788 ± 0.013	12.806 ± 0.011	12.103 ± 0.011	11.355 ± 0.020